Astronomy & Astrophysics manuscript no. Alcala˙GHOST˙Macc˙pilot˙2col˙corr
June 22, 2021
© ESO 2021

arXiv:2106.10724v1 [astro-ph.SR] 20 Jun 2021

GIARPS High-resolution Observations of T Tauri stars (GHOsT). III. A pilot study of stellar and accretion properties ⋆

J.M. Alcalá[1], M. Gangi[2], K. Biazzo[2], S. Antoniucci[2], A. Frasca[3], T. Giannini[2], U. Munari[4], B. Nisini[2], A. Harutyunyan[5], C. F. Manara[6], and F. Vitali[2]

[1] INAF-Osservatorio Astronomico di Capodimonte, via Moiariello 16, 80131 Napoli, Italy
[2] INAF-Osservatorio Astronomico di Roma, Via di Frascati 33, 00078 Monte Porzio Catone, Italy
[3] INAF-Osservatorio Astrofisico di Catania, via S. Sofia 78, 95123 Catania, Italy
[4] INAF-Osservatorio Astronomico di Padova – Via dell'Osservatorio 8, 36012, Asiago (VI), Italy
[5] Fundación Galileo Galilei – INAF – Telescopio Nazionale Galileo, 38700, Breña Baja, Santa Cruz de Tenerife, Spain
[6] European Southern Observatory, Karl Schwarzschild Str. 2, 85748 Garching, Germany

Received ; accepted

ABSTRACT

The mass-accretion rate, $\dot{M}_{\rm acc}$, is a crucial parameter for the study of the evolution of accretion disks around young low-mass stellar objects (YSOs) and for planet formation studies. The Taurus star forming region (SFR) is rich in pre-main sequence (PMS) stars, most of them of the T Tauri class. A variety of methodologies have been used in the past to measure mass accretion in samples of YSOs in Taurus, but despite being a general benchmark for star formation studies, a comprehensive and systematic analysis of the Taurus T Tauri population, where the stellar and accretion properties are derived homogeneously and simultaneously, is still missing. As part of the GIARPS High-resolution Observations of T Tauri stars (GHOsT) project, here we present a pilot study of the stellar and accretion properties of seven YSOs in Taurus using the spectrograph GIARPS at the Telescopio Nazionale Galileo (TNG). Contemporaneous low-resolution spectroscopic and photometric ancillary observations allow us to perform an accurate flux calibration of the high-resolution spectra. The simultaneity of the high-resolution, wide-band spectroscopic observations, from the optical to the near-infrared (NIR), the veiling measurements in such wide spectral range, and many well-calibrated emission line diagnostics allows us to derive the stellar and accretion properties of the seven YSOs in a homogeneous and self-consistent way. The procedures and methodologies presented here will be adopted in future works for the analysis of the complete GHOsT data set. We discuss the accretion properties of the seven YSOs in comparison with the 90% complete sample of YSOs in the Lupus SFR and investigate possibilities for the origin of the continuum excess emission in the NIR.

Key words. Stars: pre-main sequence, low-mass – Accretion, accretion disks – protoplanetary disks – stars: variables: T Tauri – individual objects: RY Tau, DG Tau, DL Tau, HN Tau A, DO Tau, RW Aur A, CQ Tau

1. Introduction

The way in which circumstellar disks evolve and form protoplanets is deeply influenced by the processes of mass accretion onto the star, ejection of outflows, and photo-evaporation of disk material through winds (Hartmann, Herczeg & Calvet 2016; Ercolano & Pascucci 2017, and references therein). In order to understand planet formation it is necessary to explain how optically thick accretion disks surrounding the youngest low-mass ($M_\star \lesssim 2.0 M_\odot$) stars evolve into optically thin debris disks (Morbidelli & Raymond 2016). In this framework, the mass accretion rate, $\dot{M}_{\rm acc}$, is a fundamental parameter for the evolution of accretion disks around young low-mass stellar objects (YSOs). $\dot{M}_{\rm acc}$ measurements set important constraints for disk evolution models (Hartmann et al. 1998; Hartmann, Herczeg & Calvet 2016) and disk clearing mechanisms (Alexander et al. 2014; Ercolano & Pascucci 2017, and references therein).

In the current magnetospheric accretion paradigm for classical T Tauri (CTT) stars , the strong stellar magnetic fields truncate the inner disk at a few stellar radii (Donati & Landstreet 2009; Johns-Krull et al. 2013). Gas flows from this truncation radius onto the star along the stellar magnetic field lines, crashing onto the star and forming an accretion shock. The $\sim 10^4$ K optically thick post-shock gas and optically thin pre-shock gas produce emission in the Balmer and Paschen continua and in many lines, including the Balmer and Paschen series and the Ca II IR triplet (Hartmann et al. 1998; Hartmann, Herczeg & Calvet 2016) observed in the optical spectra of CTTs.

The mass accretion rate can be derived from the energy released in the accretion shock (accretion luminosity $L_{\rm acc}$; see Gullbring et al. 1998; Hartmann 1998) given the stellar properties. Observationally, this requires measurements of excess flux in continuum and lines with respect to similar nonaccreting template stars. Such measurements are best performed at ultraviolet (UV) wavelengths ($\lambda \lesssim 4000$ Å) with the Balmer continuum excess emission and the Balmer jump (see Herczeg & Hillenbrand 2008; Ingleby et al. 2013; Alcalá et al. 2014, 2017; Manara et al. 2017a, and references therein). In the past, $L_{\rm acc}$ has been calculated using veiling measurements in high-resolution optical spectra (e.g., Hartigan et al. 1991; Hartigan & Kenyon 2003; White & Hillenbrand 2004, and references therein). Also, it is well known that $L_{\rm acc}$, and therefore $\dot{M}_{\rm acc}$, is correlated with the line luminosity, $L_{\rm line}$, of H I, He I, and Ca II lines (e.g.,

Send offprint requests to: J.M. Alcalá

⋆ Based on observations made with the GIARPS instrument at the Telescopio Nazionale Galileo under program A36TAC_22 (PI: Antoniucci).

Correspondence to: juan.alcala@inaf.it

Muzerolle et al. 1998; Calvet et al. 2004; Herczeg & Hillenbrand 2008; Rigliaco et al. 2012; Alcalá et al. 2014, 2017, and references therein). These latter works provide $L_{\rm acc}$–$L_{\rm line}$ correlations simultaneously and homogeneously derived from the UV to the near-infrared (NIR), underlying the importance of these emission features as accretion diagnostics. These accretion tracers are key diagnostics with which to estimate $L_{\rm acc}$via the correlations mentioned above when flux-calibrated spectra below λ~3700 Å are missing.

On the other hand, accretion is a highly variable process (Basri & Batalha 1990; Jayawardhana et al. 2006; Cody & Hillenbrand 2010; Venuti et al. 2014), which leads to a range of $\dot{M}_{\rm acc}$ values for a given object when measured at different epochs (see Costigan et al. 2012, 2014; Biazzo et al. 2012). Variability in YSOs induces dispersion in the observed $\dot{M}_{\rm acc}$–$M_\star$ and $\dot{M}_{\rm acc}$–$M_{\rm disk}$ scaling relationships, but cannot explain the large scatter of more than 2 dex in $\log \dot{M}_{\rm acc}$ at a given YSO mass. Such scaling relationships are predicted by the theory of viscous disk evolution (Lynden-Bell & Pringle 1974; Hartmann, Herczeg & Calvet 2016; Rosotti et al. 2017, and references therein), but the $\dot{M}_{\rm acc}$–$M_{\rm disk}$ relationship has been confirmed observationally only recently by spectroscopic surveys in strong synergy with ALMA surveys of disks in star forming regions (Ansdell et al. 2016; Manara et al. 2016; Pascucci et al. 2016; Mulders et al. 2017).

As concluded in previous works (e.g., Rigliaco et al. 2012; Alcalá et al. 2014), the average $L_{\rm acc}$ and $\dot{M}_{\rm acc}$ derived from several diagnostics, measured simultaneously, has a significantly reduced error. This suggests the need to use spectroscopic observations simultaneously performed from visible to NIR wavelengths and with the highest possible resolution to overcome problems due to line blending. These requirements can be achieved with the GIARPS (GIAno and haRPS, Claudi et al. 2017) high-resolution spectrograph at the Telescopio Nazionale Galileo (TNG) in the Canary Islands, Spain. The spectral coverage and resolution of GIARPS allows one to probe the properties of the accretion columns, hot spots, the inner gaseous disk, the stellar and disk winds, and the collimated jets (see Gangi et al. 2020; Giannini et al. 2019), making TNG/GIARPS a powerful instrument with which to investigate accretion in YSOs of the northern hemisphere, such as the Taurus-Auriga star forming region (SFR).

The Taurus SFR contains a rich population of pre-main sequence (PMS) stars, most of them T Tauri stars (see Kenyon et al. 2008, and references therein). Several works have addressed the problem of measuring $\dot{M}_{\rm acc}$ in the Taurus population using the different methodologies mentioned above (see Herczeg & Hillenbrand 2008, 2014, and references therein). Also, a large number of CTTs have already been observed with ALMA (Andrews et al. 2018; Long et al. 2019), probing the outer regions of their disk, and allowing the scaling relationships predicted by the viscous disk evolution theory to be investigated further. However, despite being a general benchmark for star formation studies, a comprehensive and systematic analysis of the Taurus population, where the relevant stellar and accretion parameters are derived simultaneously with sufficient accuracy, is still missing. As a first step in filling this gap, here we present a pilot study of the accretion of seven YSOs in Taurus observed with TNG/GIARPS as part of the GHOsT (GIARPS High-resolution Observations of T Tauri stars) project. GHOsT is a survey of a flux-limited complete sample of T Tauri stars in the Taurus star forming region that is to be used to derive, in a homogeneous fashion (thus avoiding systematic errors due to the use of different sets of nonsimultaneous observations), the stellar, accretion, and outflow parameters, and to constrain the properties of both the inner disk and the associated winds and jets. The ultimate goal of GHOsT is to provide reliable measures of the mass-accretion and mass-loss rates of the Taurus population and to put them in relation with the properties of the central star and its disk, in synergy with the complementary ALMA observations (Andrews et al. 2018; Long et al. 2019).

A comprehensive study of the jet line emission of the targets investigated in this paper was published by Giannini et al. (2019, henceforth Paper I) and an investigation of the link between atomic and molecular winds was published in Gangi et al. (2020, henceforth Paper II), while the results of the complete GHOsT survey will be presented in forthcoming papers. One of the main goals of the present paper is the definition and assessment of the methodologies for the determination of the stellar and accretion properties, in a homogeneous and self-consistent way, to be adopted for the analysis of the complete set of GHOsT data.

The paper is organized as follows. In Sect. 2 we present the target selection, the observations, and the data processing. In Section 3 we show the procedures used for the determination of the stellar parameters, and veiling estimates both in the optical and in the NIR. In Sect. 4 the methodologies to derive the accretion parameters are presented, while in Sect. 5 we discuss results on the stellar and accretion properties of the studied sample, comparing with those of the 90% complete sample of Lupus YSOs. The results of the veiling measurements are also reported and discussed in the same section. Conclusions are outlined in Sect. 6.

2. Target selection, observations, and data processing

The targets, observations, and data reduction are extensively described in Paper I and Paper II, and are briefly summarized in this section.

2.1. The targets

For the pilot study, we selected six well-known CTTs in Taurus-Auriga with clear signatures of accretion. The sources are listed in Table 1 together with relevant properties from the literature (see also Paper I). Noteworthy is the range of values for both the stellar physical parameters and mass accretion rate, which is likely due to variability, but also to the distinct methodologies used to derive them in previous works. The extreme CTT RW Aur A (Alencar et al. 2005) was included in the sample as a case of highly veiled object spectrum (Herczeg & Hillenbrand 2014) to test the limits of our procedures. In addition, we also study the well-known intermediate-mass CTT CQ Tau. This object was recently investigated in detail with ALMA (Ubeira Gabellini et al. 2019) and has a low level of accretion (e.g., Mendigutía et al. 2011); therefore, it has been included to test the ability of our methods to trace very low accretion rates. However, this object displays a remarkable UX Ori-type variability (Shakhovskoj et al. 2005), which complicates the analysis of the data (Dodin & Suslina 2021). Several of the selected CTTs have been included in the recent ALMA survey by Long et al. (2019). Hereafter, we use the terms CTT and YSO interchangeably to refer to the objects in our sample.

Table 1. Selected CTTs for this study with their physical and accretion properties from the literature.

Source	SpT	$T_{\rm eff}$ (K)	$A_{\rm V}$ (mag)	$L_\star$ ($L_\odot$)	$R_\star$ ($R_\odot$)	$M_\star$ ($M_\odot$)	Ref.	$\log\dot{M}_{\rm acc}$ ($M_\odot$ / yr)	Method for $\dot{M}_{\rm acc}$ determination	Ref. $\dot{M}_{\rm acc}$	d (pc)
RY Tau	G1	5945	2.20	9.60	2.9	2.00	1	−7.04/−7.19	UV-excess	1	138
		5750	0.6-1.7	6.30		1.90	2	−7.30		15	
	F7	6220	1.95	12.30		2.04	6				
		5920	2.35				18	−7.21	Hα, He I6678	18	
	K1	5080		7.60	2.92	2.00	19	−7.11	Hα	19	
DG Tau	K7.0		1.60	0.51		0.76	3	−8.20	Hα	3	125
	K6						17	−7.00	Brγ	4	
								−6.30	UV-excess	5	
		4350	2.20				18	−7.30	Hα, He I6678	18	
	M0	3890		1.70	2.87	0.30	19	−6.39	Hα	19	
	K3	4775		3.62	2.80	2.20	20	−6.13	Excess emiss.	21	
DL Tau	K5.5	4277	1.80	0.65		0.98	6	−8.6	Hα	3	160
	K5.5		1.80	0.50		0.92	3	−6.3	UV-excess	5	
						0.75	16				
HN Tau A	K3		1.15	0.17		0.70	3	−8.69	Hα	3	134
	K3	4730	1.15	0.16		1.53	6	−8.89	UV-excess	7	
	K5		0.65	0.19	0.76	0.81	7	−8.37	Several line lum.	8	
						0.78	16				
DO Tau	M0		2.27	1.01	2.25	0.37	7	−6.84	UV-excess	7	139
	M0.3	3806	0.75	0.23		0.59	6	−8.21	Hα	3	
						0.56	16				
RW Aur A	K3		0.5	0.50	1.10	0.90	9	−7.70	UV-excess	9	183
	K0-K3	5082	0.4	1.70		1.34	10	−7.50	UV-excess	10	
	K0	5250	0.0	0.99		1.20	6	−7.39	Several line lum.	11	
	K2	4955		1.70	1.70	1.34	20	−7.51	Excess emiss.	21	
CQ Tau	F2		1.90	10.0		1.67	12	< -8.3	UV-excess	13	149
								−7.0	Brγ	14	
	F3	6900	1.40	3.4			22				

Notes.
– Parameters of Long et al. are revisited values of Herczeg & Hillenbrand (2014).
– $A_{\rm V}$, SpT, $L_\star$ in Simon et al. (2016) are those in Herczeg & Hillenbrand (2014).
– Distances in the last column are from Gaia EDR3 (Gaia Collaboration et al. 2016a, 2020b).

References:
(1) Calvet et al. (2004); (2) Garufi et al. (2019); (3) Simon et al. (2016); (4) Agra-Amboage et al. (2011); (5) Gullbring et al. (2000); (6) Long et al. (2019); (7) Gullbring et al. (1998); (8) Fang et al. (2018); (9) Ingleby et al. (2013); (10) White & Genz (2011); (11) Facchini et al. (2016); (12) Ubeira Gabellini et al. (2019); (13) Mendigutía et al. (2011); (14) Donehew & Brittain (2011); (15) Skinner et al. (2018);(16) Rigliaco et al. (2015); (17) Hessman & Guenther (1997); (18) Frasca et al. (2018); (19) Isella et al. (2009, and references therein); (20) Akeson et al. (2005, and references therein); (21) White & Hillenbrand (2004); (22) Meeus et al. (2012).

2.2. Observations and data reduction

The GIARPS observing mode combines the HARPS-N (Pepe et al. 2002; Cosentino et al. 2012) and GIANO-B (Oliva et al. 2012; Origlia 2014) high-resolution (resolving power of 115,000 and 50,000, respectively) spectrographs, simultaneously covering a wide spectral range of 390–690 nm for HARPS-N, and 940–2420 nm for GIANO-B. In order to perform a flux calibration as accurately as possible, avoiding additional uncertainties due to variability, the GHOsT survey is complemented with simultaneous/contemporaneous (within less than two days of the GIARPS observations) low-resolution spectroscopy in the optical, as well as with optical and NIR photometry (see Paper I).

The TNG/GIARPS observations were performed in 2017 during two nights, one on October 29 and the other on November 13. The journal of the GIARPS observations is reported in Paper I. The reduction steps of the GIARPS spectra are thoroughly described in Paper I and Paper II, but a summary is provided here.

The HARPS-N spectra were reduced using the latest version (Nov. 2013) of the HARPS-N instrument Data Reduction Software and applying the appropriate mask depending on the spectral type of the object (Pepe et al. 2002). The basic processing steps for the data reduction consist in bias and dark subtraction, flat fielding, wavelength calibration, spectrum extraction, and cross-correlation computation. For the removal of the spurious features caused by the telluric lines we first used the *molecfit* tool (Smette et al. 2015; Kausch et al. 2015) to produce a synthetic telluric spectrum and then the package *telluric* in IRAF[1] to remove the telluric lines.

In order to flux-calibrate the HARPS-N spectra, the contemporaneous absolute flux-calibrated spectroscopy was acquired within 2 nights of our GHOsT runs with the 1.22m telescope at the Asiago observatory, Italy. The spectra cover the wavelength range 330–790 nm and were fully reduced and flux-calibrated against a spectrophotometric standard observed during the same night. Their flux zero-point was also checked with BVR_CI_C photometric measurements collected during the same nights with the ANS Collaboration telescopes (see Munari et al. 2012). The photometry is reported in Paper I. Given the short temporal distance

[1] IRAF is distributed by the National Optical Astronomy Observatory, which is operated by the Association of the Universities for Research in Astronomy, inc. (AURA) under cooperative agreement with the National Science Foundation.

between the two datasets we assume that the continuum shape did not change significantly between the Asiago and TNG observations. Thus, for each source we first fitted the continuum of the Asiago spectrum and then multiplied it for the continuum-normalized HARPS-N spectrum.

The GIANO-B spectra were extracted following the data-reduction prescriptions described in Carleo et al. (2018). Halogen lamp exposures were employed to map the order geometry and for flat-field correction, while wavelength calibration was based on lines from a U-Ne lamp acquired at the end of each observing night. The *molecfit* tool (Smette et al. 2015) was used for removing the telluric contribution in the near infrared.

To flux-calibrate the GIANO-B spectra, NIR photometry in the JHK_S bands was acquired with the REMIR instrument on the Rapid-Eye-Mount (REM) telescope (Vitali et al. 2003), at the La Silla Observatory, Chile, during the night of November 11, 2017. We assume that the NIR magnitudes did not change significantly between TNG, Asiago, and REM observations. We then performed an interpolation between the considered flux measurements using a spline function to derive a smooth continuum function in the wavelength range 940–2420 nm, that is a response function, which was then applied to flux-calibrate the various (continuum-normalized) segments of the GIANO-B spectrum. Finally, the flux-calibrated spectral segments most relevant for this pilot study of accretion were selected.

We estimate that the flux calibration of the GIARPS spectra is precise within 20%. The final products do not contain the region of the Balmer Jump, but include 17 well-resolved accretion diagnostics (12 in the optical and 5 in the NIR) that form the basis for our measurements of accretion in the sample (see Sect. 4).

3. Stellar parameters

A first step in any study of accretion is the determination of the YSO physical properties. Estimates of the physical parameters, derived using a number of methodologies, exist in the literature for all the YSOs in our sample. In order to minimize uncertainties due to the different procedures used in the literature, and in view of the forthcoming GHOsT data, we need to adopt a methodology that allows us to determine the YSO properties in a self-consistent and homogeneous way.

3.1. Effective temperature and optical veiling

We used the ROTFIT code to determine effective temperature, $T_{\rm eff}$, surface gravity, $\log g$, radial velocity, RV, projected rotational velocity, $v \sin i$, and veiling as a function of wavelength, r_λ. The code has been successfully applied on YSOs optical spectra at different resolutions (Frasca et al. 2006, 2015), and is particularly well suited for the HARPS-N spectra. In short, the code finds the best photospheric rotationally broadened template spectrum that reproduces the target spectrum by minimizing the χ^2 of the difference between the observed and template spectra in specific spectral segments. The spectral segments ($\sim$ 100 Å each) are normalized to unity, and therefore a measure of extinction is not provided by the code. We adopted as templates a grid of high-resolution spectra of slowly rotating, low-activity stars with well-known atmospheric parameters, which were retrieved from the ELODIE Archive (Moultaka et al. 2004). The HARPS-N spectra were degraded to the ELODIE resolution ($R = 42,000$) before running the analysis code. We have chosen this template grid because real spectra are best suited for the determination of veiling and $v \sin i$ (Frasca et al. 2015, 2019). Moreover, they allow us to perform a careful subtraction of the photospheric spectrum (see Section 4.1). The spectral intervals analyzed with ROTFIT contain features that are sensitive to the effective temperature and/or $\log g$.

The whole set of physical parameters derived with ROTFIT ($T_{\rm eff}$, $\log g$, RV, $v \sin i$, and veiling) for the complete GHOsT sample will be presented in a forthcoming paper, while the effective temperature, essential for this work, is provided in Table 2. Optical veiling values, also crucial for this pilot study, are given in Table 3. The spectral types, determined using the $T_{\rm eff}$ from ROTFIT and the relation between spectral type versus $T_{\rm eff}$ by Herczeg & Hillenbrand (2014), are also reported in column 3 of Table 2.

For RW Aur A it was not possible to derive the parameters using the ROTFIT method, as the spectrum is totally crossed by emission lines that hide the photospheric lines at optical wavelengths. As discussed in Sect. 3.2, the templates best matching the NIR spectrum have a spectral type between K1 and K0, the latter being consistent with the determination by Herczeg & Hillenbrand (2014) for this star. We therefore adopted the $T_{\rm eff}$ value as determined from the K0 spectral type and the SpT versus $T_{\rm eff}$ relationship by these authors. For this star, Herczeg & Hillenbrand (2014) report a veiling of 0.5 at λ =750 nm. Based on a linear relationship between the veiling at 580 nm and 710 nm drawn from our previous studies of the Lupus population (Alcalá et al. 2014, 2017), we estimate that the veiling at λ =600 nm is $r600 \approx 2.3 \times r710$, where r710 is the veiling at λ =710 nm. Within the errors, this is consistent with the measured veiling in Frasca et al. (2017) where $r620 \approx 2.0 \times r710$. For RW Aur A, we calculate a value of $r600 \sim 1.2$. We find a similar value of veiling considering the equivalent width of the lithium line at 6708 Å and applying the method described in Biazzo et al. (2011). However, we consider this a tentative value only, as the veiling of this CTT may be strongly variable ($0.3 < r_\lambda < 6.1$, for λ in the range 500–650 nm, Stout-Batalha et al. 2000).

The corresponding $T_{\rm eff}$ values derived from ROTFIT are in good agreement, within the errors, with those drawn from the Herczeg & Hillenbrand (2014) spectral types. As a logical consequence, the spectral types are also in good agreement, within a spectral subclass. We note that the values for CQ Tau, which have not been included in the Herczeg & Hillenbrand (2014) study, are in agreement with those published in Mendigutía et al. (2011) and Meeus et al. (2012). Also, the negligible veiling at optical wavelengths for this star is in agreement with the recent results by Dodin & Suslina (2021).

3.2. Veiling and $v \sin i$ estimates in the NIR

The veiling of IR photospheric lines is usually attributed to the emission of the inner edge of the dusty disk, where the dust is heated by stellar and accretion radiation. As such, it can be used to infer properties of the emission in excess of the stellar photosphere originating in the inner disk and complementary to the UV and optical excess. In addition, veiling may have an important impact on extinction (see Fischer et al. 2011; Herczeg & Hillenbrand 2014, and references therein).

The procedure we used to measure veiling of the photospheric lines in the NIR follows the prescription thoroughly described in Antoniucci et al. (2017). Briefly, we use template spectra acquired with GIANO-B and with similar spectral types to the targets. The templates are chosen to have very low $v \sin i$ values. Each template spectrum is broadened by convolution

Table 2. Properties of the CTT sample derived in this work

Name	$T_{\rm eff}$ (±err) (K)	SpT	$A_{\rm V}$ [a] (mag)	$A_{\rm V}$ [b] (mag)	$L_\star$ ($L_\odot$)	$R_\star$ ($R_\odot$)	$M_\star$ ($M_\odot$)
(1)	(2)	(3)	(4)	(5)	(6)	(7)	(8)
RY Tau	5856 (151)	G1	2.25	2.32	8.87	2.89	1.80
DG Tau	4004 (153)	K7	1.50	1.79	0.44	1.38	0.70
DL Tau	4188 (100)	K5	1.50	1.45	0.40	1.20	0.90
HN Tau A†	4617 (97)	K4	1.25	1.53	0.15	0.60	0.80⋆
DO Tau	3694 (104)	M1	1.40	1.69	0.42	1.58	0.50
RW Aur A	4870	K0	1.00	0.57	1.64	1.80	1.50
CQ Tau‡	6823 (136)	F4	0.50	0.60	2.71	1.18	1.50⋆

Notes.
[a]: extinction derived using spectral templates only.
[b]: extinction derived using spectral templates and veiling.
† : subluminous YSO (Sect. 3.4). The $L_\star$, $R_\star$, and $M_\star$ values are underestimated.
‡ : UX Ori type variable (Sect. 3.4). Parameters affected by variable circumstellar extinction.
⋆: corrected values of $L_\star$, $R_\star$, and $M_\star$ for the two subluminous objects are estimated in Sect. 4.3.1. The mass reported here is that of the closest PMS track on the HR diagram, with the uncorrected values of $L_\star$.

Table 3. Veiling in the optical from ROTFIT and in the NIR with the procedure described in text. The projected rotational velocity determined with this procedure is also given in the last column.

Name	*r*450	*r*500	*r*550	*r*600	*r*650	*r*968	*r*983	*r*1178	*r*1256	*r*1298	*r*1565	*r*1597	*r*1666	*r*1741	*r*2130	*r*2255	*r*2322	$v \sin i$ (±err) (km/s)
RY Tau	0.0	0.0	0.0	0.0	0.0	0.2	0.6	0.4	0.7	0.3	0.5	0.4	0.5	0.9	1.4	1.2	...	49.8 (1.6)
DG Tau	...	...	2.0	1.5	1.0	1.6	1.2	1.8	1.4	1.7	1.8	1.6	1.7	2.4	3–4	3–4	...	26.3 (3.3)
DL Tau	3.0	2.5	2.0	1.2	1.5	1.1	1.1	1.1	1.0	1.0	0.9	0.6	0.8	1.7	2.5	2.1	2.5	12.0 (3.0)
HN Tau A	...	0.8	0.8	0.8	0.5	...	...	1.1	1.2	1.5	1.8	1.6	1.3	2.3	3.3	5.0	...	50.7 (2.7)
DO Tau	1.8	1.5	1.5	1.0	1.5	0.5	0.6	0.7	1.4	1.4	1.9	1.7	1.8	2.1	3.4	3.7	2.7	12.0 (2.2)
RW Aur A	...	...	...	1.2	...	...	...	...	1.5	...	...	2.5	2.7	3.5	3.6	5.7	5.4	20.0 (3.4)
CQ Tau	0.0	0.0	0.0	0.0	0.0	...	0.5	1.0	0.8	...	<3.0	2.0	...	...	...	...	...	79.0 (5.0)

with a rotational profile (Gray 2005) by increasing $v \sin i$ and it is artificially veiled by adding a continuum excess, with both $v \sin i$ and r_λ as free parameters (see Eq. 1 in Antoniucci et al. 2017), until the photospheric features match those of the target and minimum residuals between the target spectrum and the rotationally broadened and veiled template are obtained. Figure 1 shows an example of the result of the fitting procedure for HN Tau A in two spectral intervals. The r_λ values are assumed to be constant within each spectral order. Values of r_λ derived from this procedure are given in Table 3. The procedure also yields an estimate of $v \sin i$, which is also given in Table 3. The errors in veiling are on the order of 20%.

As mentioned in the previous section, the optical HARPS-N spectrum of RW Aur A is heavily veiled and crossed by numerous emission lines. Yet its NIR GIANO-B spectrum shows some photospheric lines making it possible to estimate veiling and $v \sin i$. During this process, we were also able to determine that the spectral type of the template best matching the photospheric lines corresponds to a type between K1 and K0. We stress that in the case of DG Tau, the *r*2130 and *r*2255 estimates are rather uncertain, and so we were only able to determine a range of values (see Table 3).

3.3. Extinction

As a first step to derive the visual extinction, $A_{\rm V}$, we adopt the methods described in our previous works (Alcalá et al. 2014, 2017; Manara et al. 2017a). As input data we use our primary flux calibrated spectra, that is the Asiago spectra, which cover a sufficient wavelength range (330–790 nm) for the purpose. To derive $A_{\rm V}$ for a given YSO, its spectrum was compared with the spectra of nonaccreting YSOs best matching in spectral type. All our nonaccreting templates were taken from Manara et al. (2013, 2017) and have very low or negligible extinction ($A_{\rm V} < 0.5$ mag; see Manara et al. 2013, 2017). The templates were rebinned to the Asiago spectra and then artificially reddened by $A_{\rm V}$ in the range 0.0–4.0 mag in steps of 0.25 mag until the best match to the continuum slope of the YSO spectrum was found. To redden the spectra we used the extinction law by Weingartner & Draine (2001) for $R_{\rm V} = 5.5$, which has been found to be particularly well suited for YSOs in general (Evans et al. 2009, and references therein). The $A_{\rm V}$ values derived in this way are listed in column 4 of Table 2.

The main sources of uncertainty on $A_{\rm V}$ are the errors in spectral type when associating a template to a given YSO, the error in the extinction of the templates, and the errors in flux calibration. The combined effect leads to an error of ∼0.35 mag, except for the case of RW Aur A for which we estimate a larger error of about 0.5 mag. Adopting extinction laws by different authors yields results consistent, within the errors of about 0.35 mag, with those of Herczeg & Hillenbrand (2014). For instance, the latter authors find that for a star with their measured $A_{\rm V}$=1.0 mag, adopting $R_{\rm V}$ =5 from Cardelli et al. (1989) or $R_{\rm V}$ =5.1 from Weingartner & Draine (2001) would yield $A_{\rm V}$= 1.2 and 1.15 mag, respectively.

As mentioned in Section 3.2, another source of uncertainty is strong veiling, which makes the YSO spectra intrinsically bluer than the templates. The extinction as derived above is not severely affected by the veiling, as soon as the analysis is restricted to wavelengths longer than about 450 nm (see analysis

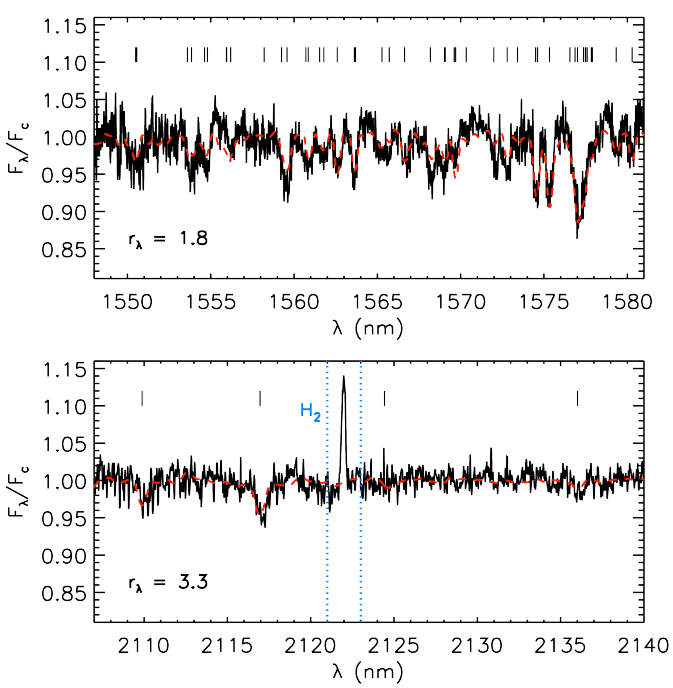


Fig. 1. Two portions of the continuum-normalized spectrum of HN Tau A (black solid line) in the *HK* bands, with the rotationally broadened and veiled spectrum of the stellar template overplotted (red dashed line). Absorption features, mainly of the iron-peak group, are indicated with small vertical lines. We refer to Rayner et al. (2009) for the details on the absorption features. Emission lines such as the H_2 line, indicated with the blue dotted lines, are excluded from the analysis. The value of veiling, which minimizes residuals with respect of the rotationally broadened and veiled template, is indicated in the lower left.

in Appendix B of Alcalá et al. 2014), but also shorter than about 800 nm to avoid the effects of veiling in the NIR (Fischer et al. 2011). Thus, to minimize the impact of veiling, the extinction was derived only from the red portion of the Asiago spectra, starting at 500 nm. In this case, the effects of NIR veiling are automatically excluded as the Asiago spectra do not cover wavelengths longer than 790 nm.

We also applied an alternative method to derive A_V using the prescription explained in Fischer et al. (2011, see their Eq. 4), originally proposed in Gullbring et al. (1998, their Eq. 5). This requires measurements of the veiling, r_λ, of the observed flux of the spectral template, F_λ^T, and of the observed flux of the object, F_λ^O, as a function of wavelength. The method is based on the fact that the quantity $\Gamma_\lambda = 2.5 \cdot \log[(1 + r_\lambda) \cdot F_\lambda^T / F_\lambda^O]$ is a linear function of the extinction curve, A_λ/A_V, and is equal to $A_\lambda/A_V \cdot (A_V{}^O - A_V{}^T) - 2.5 \cdot \log C$, where $A_V{}^O$ and $A_V{}^T$ are the visual extinction of the object and template, respectively, and C is a constant. The slope of a linear fit to the Γ_λ versus (A_λ/A_V) relationship yields the difference between the extinction of the object and the template, assuming the same extinction law for both. In our case, $A_V{}^T$ is always very close to zero and therefore the slope of the linear fit yields $A_V{}^O$.

Figure 2 shows the plots of Γ_λ versus A_λ/A_V for the YSOs in the sample. For every YSO, we used the r_λ values of Table 3, and the corresponding continuum F_λ^T and F_λ^O values reported in Tables A.1–A.7 in Appendix A. In these tables, we also report the r_λ values for convenience. The plots show the best linear fit and the corresponding slope $A_V{}^O$. The error on A_V indicated in each panel of Figure 2 is only the error on the slope of the fit and does not represent the full error on A_V, which we estimate to be also on the order of 0.35 mag based mainly on flux calibration errors and mismatch in spectral type of the templates and the CTTs. The A_V results using this method are reported in column 5 of Table 2.

In the case of RW Aur A, where the fit is not well constrained because only one rough estimate of veiling in the optical was possible, the error may be as high as 0.5 mag. Nevertheless, the resulting extinction values as derived from both methods are consistent, within the errors. We also stress that the UX Ori-type variability of CQ Tau may lead to large uncertainties on the A_V value, as part of the extinction may be gray (Dodin & Suslina 2021).

The A_V derived from the spectral templates alone and those including the veiling measurements (respectively columns 4 and 5 in Table 2) are in very good agreement within the error of about 0.35 mag, although the veiling method provides systematically higher values by up to ∼30%. As discussed in Fischer et al. (2011), the adoption of different values of the total-to-selective extinction, R_V, has little impact on the results. We adopt the A_V values derived from the "veiling" method for the subsequent analysis.

The veiling methodologies used in the NIR by Fischer et al. (2011) yielded A_V values systematically higher than those derived from other previous measurements. Yet, applying the same methods here, but extended to the optical veilings, provides A_V values that are significantly lower than those in Fischer et al. (2011) for the same stars. Herczeg & Hillenbrand (2014) also calculate much lower A_V values than Fischer et al. (2011) and interpret the higher values by the latter authors as possibly due to spectral mismatch between the templates and the CTTs and to the lower sensitivity of NIR spectra to extinction. Our extinction values are slightly higher than those of Herczeg & Hillenbrand (2014), but still consistent within the small amount of about 0.5 mag, and in some cases the agreement is very good. This is consistent with the fact that the veiling method gives A_V values that are systematically higher by ∼30% with respect to the templates method alone.

3.4. Luminosity and mass

The stellar luminosity, $L_\star$, was derived as follows. For a given object, we extracted first the BTsettl model (Allard et al. 2012) best matching the $T_{\rm eff}$ values derived with ROTFIT above (see Sect. 3.1). The model was then normalized to the extinction corrected flux, F_{600}^{corr}, of the Asiago spectrum at λ =600 nm, where the veiling estimates are expected to be more reliable, and corrections subject to less uncertainty. To take into account the contribution of veiling, the extinction-corrected flux at 600 nm was multiplied by the factor $1/(1+r600)$, where $r600$ is the veiling at λ =600 nm derived from ROTFIT and listed in Table 3 (see example for DL Tau in Figure 3). This factor, which is always ≤1, effectively reduces the observed flux to that emitted by the stellar photosphere only, excluding the emission due to accretion.

We therefore assume that the BT-settl model normalized in this way best represents the spectral energy distribution (SED) of the object's photosphere at the star distance. Integration of the normalized model at all wavelengths yields the bolometric flux corresponding to the object's photosphere. The stellar luminosity was then calculated using this flux and adopting the distance reported in Table 1. The main sources of uncertainty on

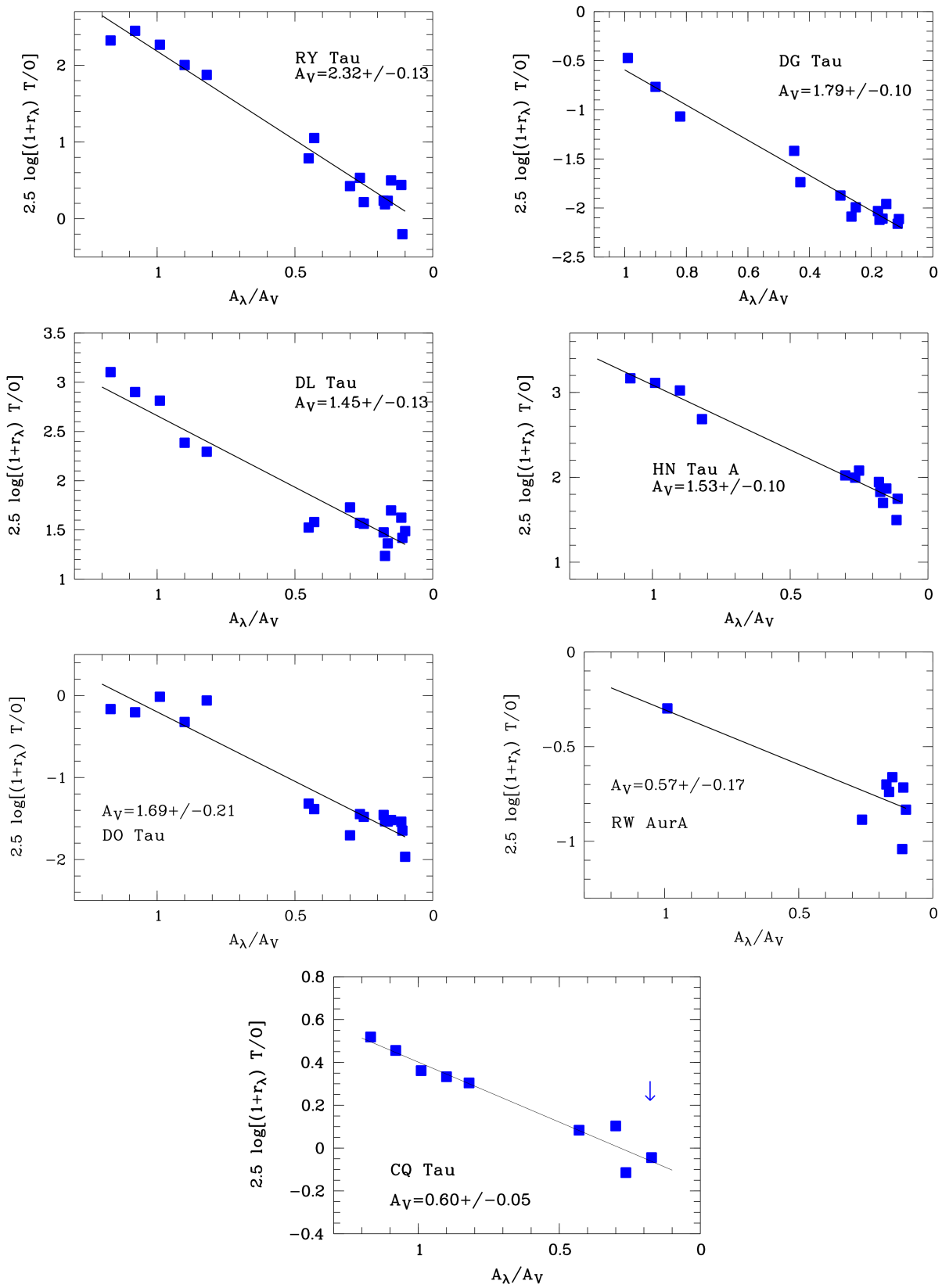


Fig. 2. Plots of $2.5 \cdot \log\left[(1 + r_\lambda) \cdot F_\lambda^T / F_\lambda^O\right]$ vs. A_λ/A_V for the YSOs in the sample (blue squares). The best linear fit for each object is shown as a black line. The value of the slope A_V is shown in each panel. In the case of CQ Tau the $r1565$ value is shown as an upper limit.

$L_\star$ are the errors in flux calibration of the Asiago spectra and the error on the veiling correction. On this basis, we estimate an average uncertainty of about 0.2 dex in log$L_\star$. We verified that using veiling values at other wavelengths yields consistent results of the veiling-corrected bolometric flux. For instance, in the case of DL Tau, which has the strongest veiling at 450 nm, we derive a corrected bolometric flux of 5×10^{-10} erg s^{-1} cm^{-2} and 4.55×10^{-10} erg s^{-1} cm^{-2} when using the r600 and r450 values, respectively. The stellar radius, $R_\star$, was calculated from the effective temperature and stellar luminosity.

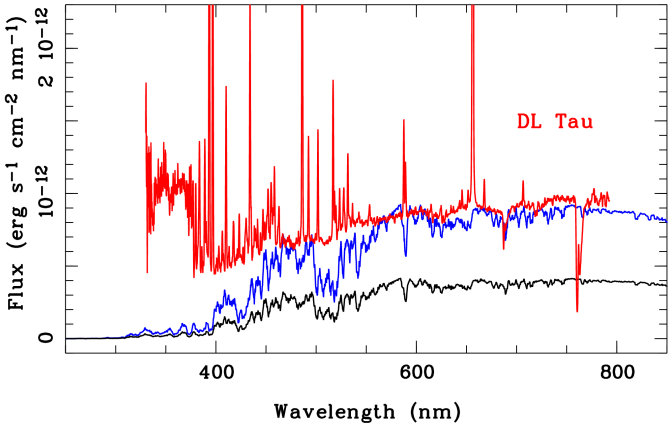


Fig. 3. Example of BT-settl model normalization. The extinction-corrected Asiago spectrum of DL Tau is shown with the red line, while the BT-settl model normalized to DL Tau at λ =600 nm is plotted with the blue line. We note the increase of excess emission of DL Tau at wavelengths shorter than about 450 nm. The veiling-corrected BT-settl model is plotted with the black line. See text for details

In some cases (e.g., DG Tau) the $L_\star$ values from the oldest literature may be overestimated most likely because such determinations did not consider the contribution of veiling and/or overestimate extinction. Our stellar luminosities are well consistent with those derived in Herczeg & Hillenbrand (2014) within the error of about 0.2 dex in log$L_\star$. It is worth noting that in the case of RY Tau our $T_{\rm eff}$, $A_{\rm V}$, and $L_\star$ values are in good agreement, within the errors, with those reported in the recent and thorough study by Garufi et al. (2019). These values are also fairly consistent with those reported in the paper by Calvet et al. (2004).

We note that HN Tau A is subluminous on the HR diagram with both the value of Herczeg & Hillenbrand (2014) for $L_\star$ and the one derived here. This is likely due to obscuration of the stellar photosphere by the highly inclined disk ($i \approx 70^\circ$; Long et al. 2019). The $L_\star$, $R_\star$, and $M_\star$ values for this star may be underestimated by a factor of ∼17, ∼4.3, and ∼2, respectively (see Sect. 4.3.1). Likewise, our derived luminosity for CQ Tau places the star slightly below the main sequence, most likely as a consequence of the fact that during the periods of dimming, the extinction may be gray, and therefore the luminosity is underestimated. The GHOsT observations of this star were performed when it was in a faint stage, that is, B =10.89 mag as compared with B =9 mag in its bright phase (Grinin et al. 2008), and therefore its luminosity may be underestimated by a factor of about six (see also Sect. 4.3.1).

Finally, the mass, $M_\star$, of the seven CTTs was estimated by comparison of the position of the objects on the HR diagram with the theoretical PMS evolutionary tracks by Siess et al. (2000). The uncertainties on $L_\star$ and $T_{\rm eff}$ lead to a typical uncertainty of ∼0.15 dex in $M_\star$. The derived $L_\star$, $R_\star$, and $M_\star$ values for the sample are given in Table 2. The mass reported in this table for the subluminous objects HN Tau A and CQ Tau corresponds to that of the evolutionary track closest to these stars on the HR diagram, but corrected values are estimated in Section 4.3.1.

4. Accretion diagnostics

The GIARPS spectra include several emission lines that are well correlated with $L_{\rm acc}$ (Alcalá et al. 2014, 2017) and will be the basis of our measurements of accretion in the sample. In particular, we extracted 17 spectral portions with well-resolved and flux-calibrated accretion diagnostics, namely, eight hydrogen recombination lines (Hα, Hβ, Hγ, Hδ, Paβ, Paγ, Paδ, Pa8), eight helium lines (He I 4026, He I 4471, He I 4713, He I 4922, He I 5016, He I 5876, He I 6678, He I 10830), and the Ca II 3934 line.

Figure 4 shows examples of GIARPS spectra for several emission lines of every CTT star in our sample. For comparison, the spectra are normalized to the local continuum and shifted in velocity to the rest wavelength. The latter was determined from the profiles of the Li I λ6708 Å photospheric line, assuming weighted λ = 670.7876nm, and in the NIR from the Al I lines at λ = 2019.884, 2116.958, 2121.396 nm. All the spectra are shown in the same velocity range for comparison.

There is a variety of line profiles with a range of widths and intensities, typical of accreting YSOs. The widest lines are from RY Tau, RW Aur A, and HN Tau A, while DG Tau and DL Tau show lines with intermediate width. The narrowest lines are from DO Tau, yet the width of the Hα line at 10% of the line peak that we measure for the latter is more than 400 km/s, pointing to significant accretion activity (White & Basri 2003; Natta et al. 2006). Within the qualitative classification scheme of the Balmer lines proposed by Antoniucci et al. (2017a), RY Tau, RW Aur A, and HN Tau A display wide and multi-peak profiles, DG Tau and DL Tau show multi-peak profiles, while DO Tau shows narrow and almost symmetric profiles. All these morphologies are displayed by the Lupus sample studied by Antoniucci et al. (2017a). Two exceptions in our sample are RY Tau and CQ Tau, where many lines are dominated by the photospheric absorption and therefore the subtraction of the photospheric spectrum is needed in order to measure the residual emission (see Sect. 4.1).

4.1. Flux and luminosity of lines

The flux at Earth in permitted lines was computed by directly integrating the GIARPS flux-calibrated spectra using the *splot* package under IRAF. Three independent measurements per line were made, considering the lowest, highest, and the middle position of the local continuum, depending on the local noise level of the spectra. The flux and its error were then computed as the average and standard deviation of the three independent measurements, respectively.

In the case of RY Tau and CQ Tau, we performed the photospheric subtraction in the following way: the spectral templates used to derive the stellar parameters and NIR veiling were artificially broadened for $v \sin i$ and veiled at the same values derived from ROTFIT and the NIR veiling procedure. The rotated and veiled templates were then subtracted from the YSO spectra. In

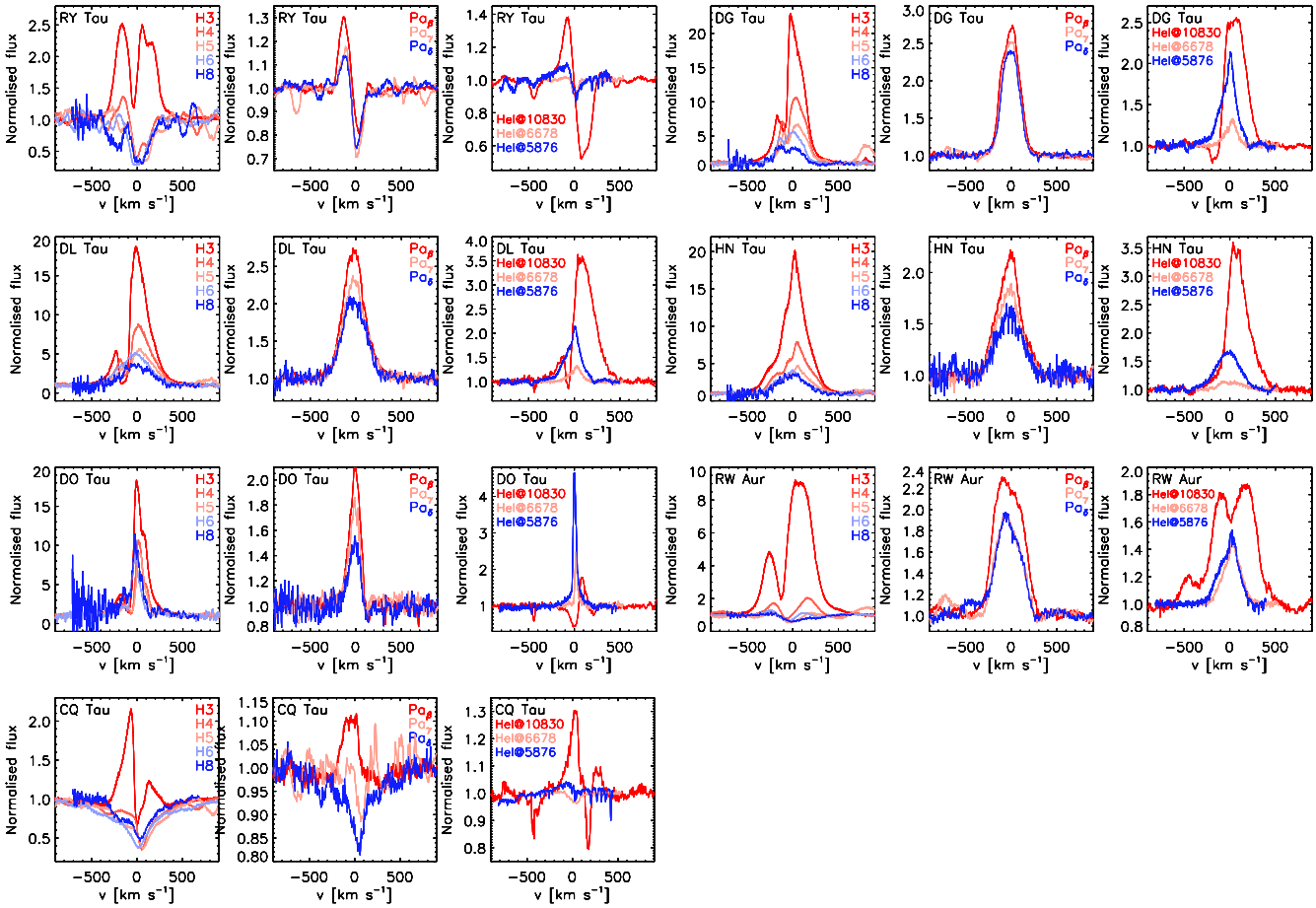


Fig. 4. Examples of GIARPS spectra showing the line profiles of CTTs in our sample

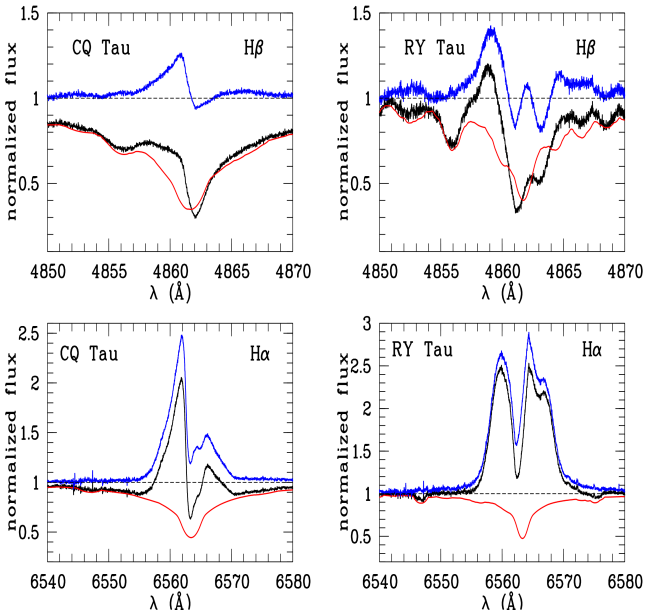


Fig. 5. Examples of photospheric line subtraction for the Hα and Hβ lines in CQ Tau and RY Tau. The black, red, and blue lines represent the observed, photospheric, and photospheric-subtracted spectra, respectively. See text for details.

this procedure, both the YSO and template spectra were normalized to the continuum around the selected lines to be analyzed. Three measurements of the equivalent widths of the corrected lines were made and the average was computed. The error was estimated by the standard deviation of the observed fluxes on the difference spectra in two spectral regions near the line. Finally, the flux of the corrected lines was computed as the product of the equivalent width times the absolute continuum flux adjacent to the lines. The procedure, illustrated in Figure 5 for the Hα and Hβ lines and in Figure 6 for the Paβ line, was applied to lines strongly affected by the photospheric contribution namely the Balmer, Paschen, and the He I λ10830 Å lines. We note that in some cases a residual contribution of nonphotospheric self-absorptions remained, in particular in the case of some Paschen and the He I λ10830 Å lines (see example in Figure 6). Lines with strong self-absorption may underestimate $L_{\rm acc}$ and therefore the measurement was not considered when such a contribution was more than ~30% of the flux. The procedure adopted here to measure the integrated flux is the same adopted in Alcalá et al. (2017), where the $L_{\rm line}$ versus $L_{\rm acc}$ calibrations were derived.

Not all the 17 lines in the GIARPS spectral range were detected or could be measured in every CTT star. A summary of the number of lines with flux measurements in every CTT in our sample is provided in the first column of Table 4, and every panel of Figure 7 shows the lines detected and measured. The absence of a point in these plots means that the line was not detected or could not be extracted with the photospheric subtraction,